Published by IOP Publishing for Sissa Medialab

Received: *February 11, 2022*
Revised: *April 6, 2022*
Accepted: *April 11, 2022*
Published: *May 23, 2022*

Radiation measurements and simulations at the PHELIX laser facility, GSI

R. Behrens,[a,*] **P. Hufschmidt,**[b] **J. Roth,**[a] **B. Akstaller,**[b] **D. Haag,**[b] **O. Hupe,**[a] **S. Schmidt,**[b] **S. Schreiner**[b] **and T. Michel**[b]

[a] *Physikalisch-Technische Bundesanstalt (PTB), 38116 Braunschweig, Germany*
[b] *Erlangen Center for Astroparticle Physics (ECAP), 91058 Erlangen, Germany*

E-mail: Rolf.Behrens@PTB.de

Abstract: The absolute spectral electron and photon emission from a Tungsten target irradiated by the Petawatt High-Energy Laser for Heavy Ion EXperiments (PHELIX) facility was measured inside the PHELIX target chamber. For this, a thermo-lumi-nescence detector (TLD)-based few-channel spectrometer (FCS) was used in combination with a Bayesian data analysis. The results of the FCS measurement served as input for a Monte-Carlo particle transport simulation to determine the spectra and dose out of the PHELIX target chamber. Two different simulation methods proved to be consistent and, therefore, reliable. The simulation results were compared to the dose measured with a dosemeter that consists of three Dosepix detectors in combination with a neural network analysis. The two dose results show a satisfactory agreement.

Keywords: Analysis and statistical methods; Detector modelling and simulations I (interaction of radiation with matter, interaction of photons with matter, interaction of hadrons with matter, etc); Dosimetry concepts and apparatus; Nuclear instruments and methods for hot plasma diagnostics

*Corresponding author.

https://doi.org/10.1088/1748-0221/17/05/P05033

2022 JINST 17 P05033

Contents

2022 JINST 17 P05033

1 Introduction

Pulsed ionizing radiation has become more prevalent in the low photon energy range up to a few hundred keV, e.g., as side effect at ultra-short, pulsed laser machines used for materials processing [1], in medical diagnostics [2], or from small, pulsed X-ray tubes for material testing such as welded seams [3], but also in the MeV range, e.g., at linear accelerators in tumor therapy [4]; even extreme laser driven radiation is investigated where energetic electrons also emerge [5]. Depending on the pulse duration, pulse structure (single or repeated, its shape etc.), dose and dose rate per pulse, neither active spectrometers nor active dosemeters function reliably [6] — e.g., due to pile-up or dead time effects. Therefore, in this work, a spectrometer based on the passive detection method of thermoluminescence dosimetry (TLD) is used [7–9]. From its readings both the absolute spectra as well as the total dose in radiation fields as described above are measured and analyzed — with the whole process of measurement and data evaluation being validated in well-defined radiation fields beforehand. The spectrometer has recently been validated and used in the low photon energy range, i.e., up to about 30 keV [10], in the medium to high photon energy range (from a few hundred keV up to a few MeV) [11], and has been used for years in the mixed electron photon high energy range at high-power laser facilities [9]. Furthermore, two active hybrid, pixelated, photon-counting X-ray detectors (Dosepix configured as a dosemeter, see below, and Timepix) are used for additional measurements [12–14]. The pixelated structure of this detector results in the advantage of much less suffering from pile-up and dead-time effects compared to other detectors. Finally, an active PIN diode was tested in the extreme radiation field.

2 Experiments

2.1 The PHEXLIX facility

The **P**etawatt **H**igh-**E**nergy **L**aser for Heavy **I**on E**X**periments (PHELIX) is a laser facility delivering very intense laser beams that can be directed onto different types of targets. Further details of the facility are available at the website of the Helmholtzzentrum für Schwerionen-forschung GmbH (GSI) [15, 16]. The experiments described in this publication took place in February 2020 during the course of an experiment for the phase-contrast imaging of a micrometer sample using the laser-driven x-ray backlighter source [17, 18]. For such experiments, the determination of the particle spectra emitted by the laser plasma has a high relevance [19]. Therefore, the spectrum and dose were measured in parallel to the experiments mentioned above and are described in this publication.

2.2 Experimental conditions

The experimental setup is shown in figure 1 while the main characteristics during the experiments are listed in table 1 and table 2. The instruments used for the measurements and radiation transport simulations performed are described in the following sections.

In total, 29 laser shots performed are considered in this publication, see table 2(a) and (b). Four different detector types were used for measuring the ionizing radiation (electrons and photons) emitted from the target, i.e., from the emerging laser plasma. Inside the target chamber a passive few-channel spectrometer (FCS) was used to measure the radiation described in section 3, its results (electron and photon spectrum) served as input for Monte Carlo transport simulations to determine

2022 JINST 17 P05033

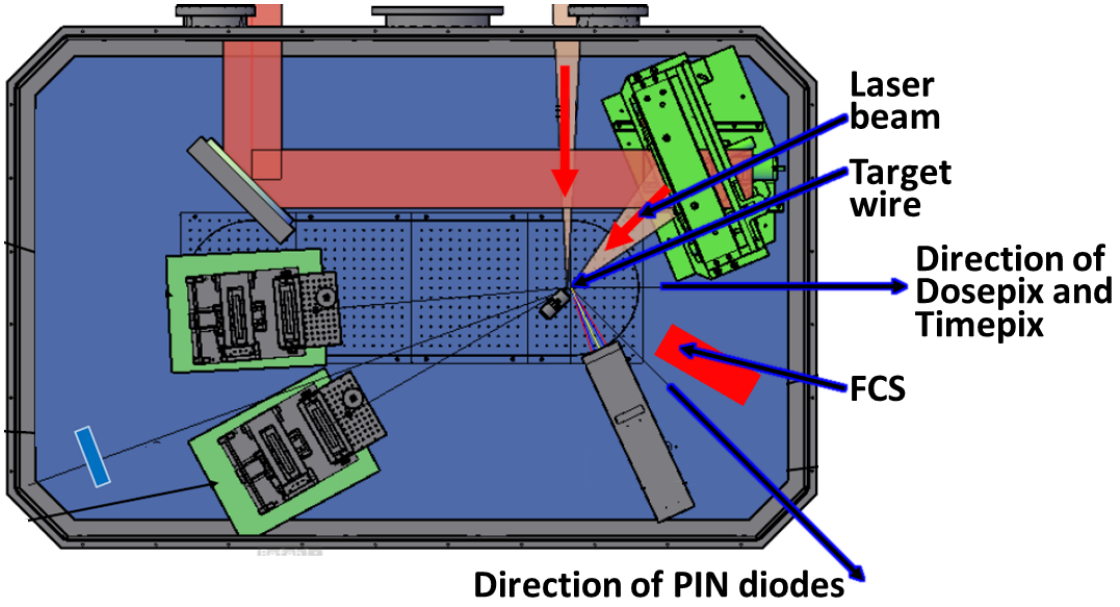

Figure 1. Sketch of experimental setup: target chamber (evacuated, $\lesssim 10^{-5}$ mbar) with the parabolic mirror to focus the laser beam (top right, green), the target wire (right center, perpendicular to the drawing plane), the few-channel spectrometer (FCS, lower right, red), and exit window in the direction of the Dosepix dosemeter and Timepix (right) and PIN diodes (bottom right). The sketch is not to scale.

Table 1. Main characteristics of the PHELIX laser facility during the experiments.

Characteristic	Value
Wavelength	1054 nm
Power	up to 500 TW
Pulse length (FWHM)	~ 500 fs
Repetition rate	~ 1 per 90 min
Focus diameter	~ 5 µm
Focus intensity	up to 10^{21} W/cm^2

the resulting radiation outside the target chamber described in section 4. Outside the target chamber the active Dosepix dosemeter, Timepix and PIN diode detectors were used to measure the radiation described in section 5. Finally, the results are presented in section 6 and some concluding remarks are given in section 7.

3 Measurements inside the target chamber

3.1 The TLD-based few channel spectrometer (FCS)

For the measurements inside the PHELIX target chamber a thermoluminescence detector (TLD)-based few-channel spectrometer (FCS) was used. TLDs, as passive detectors, are unaffected by the extremely short time structure of the radiation, and, therefore, circumvent all difficulties electronic detectors face when used in pulsed radiation fields. In the spectrometer, TLD700 detectors, i.e.,

2022 JINST 17 P05033

Table 2. Details of the experiments.

(a) Geometry and shot characteristics during the experiments (FCS and Dosepix dosemeter).

Characteristic	Few-channel spectrometer (FCS)	Dosepix dosemeter
Target material	Tungsten wire, ∅ = 5 µm or 10 µm (see below, number of laser shots)	
Angle of target wire vs. laser beam	90° vertical	
Detector location and distance	Inside target chamber 0.2 m from target	Outside target chamber 3.67 m from target
Detector direction vs. laser beam (in the plane of the laser beam)	75°	45°
Detector direction vs. laser beam (vertical to the plane of the laser beam)	0° (in the plane of the laser beam)	∼ −8° (below the plane of the laser beam)
Number of laser shots at different target wire diameters	13 (4 @ ∅ = 5 µm & 9 @ ∅ = 10 µm)	15 (8 @ ∅ = 5 µm & 7 @ ∅ = 10 µm)
	FCS and Dosepix dosemeter together: 4 (0 @ ∅ = 5 µm & 4 @ ∅ = 10 µm)	
Laser pulse energy in J/shot (mean and standard deviation of the single values)	29 ± 4	23 ± 3
	FCS and Dosepix dosemeter together: 26 ± 4	

(b) Geometry and shot characteristics during the experiments (PIN diodes and Timepix).

Characteristic	PIN diodes	Timepix
Target material	Tungsten wire, ∅ = 5 µm or 10 µm (see below, number of laser shots)	
Angle of target wire vs. laser beam	90° vertical	
Detector location and distance	Outside target chamber 1.75 m from target	Outside target chamber 3.67 m from target
Detector direction vs. laser beam (in the plane of the laser beam)	90°	45°
Detector direction vs. laser beam (vertical to the plane of the laser beam)	0° (in the plane of the laser beam)	∼ +8° (above the plane of the laser beam)
Number of laser shots at different target wire diameters	3 (2@∅ = 5 µm & 1 @ ∅ = 10 µm)	4 (all @ ∅ = 10 µm)
Laser pulse energy in J/shot (mean and standard deviation of the single values)	26 ± 4	26 ± 6

TLDs made of ^{7}LiF, were used interspaced by 30 filters made of different materials and thickness with increasing atomic number and thickness (see figure 2) [7–9]. The penetration depth of the radiation in the spectrometer depends on the type and energy resulting in the different TLD layers in increasing doses per incident fluence (response) with increasing particle energy but decreasing doses from the front to the back. The doses per incident fluence depending on the type and particle energy, i.e., the response functions, were calculated earlier [7]. By this and by taking into account further information from the experiment (see below), the energy-resolved and absolute spectra of the electron and photon radiation, including the uncertainties and coverage intervals, can be determined from the dose values in the TLD layers. The mathematical analysis to do so was performed by means of Bayesian spectrum deconvolution using the WinBUGS software [20]. The following prior information for the particle spectra was included in the data evaluation: the radiation emission consists of an electron as well as a photon contribution while i) the electron contribution consists of two Maxwellian distributions with different slopes (due to the well-known effects during the laser interaction with the target material and the emerging plasma) and ii) the photon contribution consists of two exponential decreases with different slopes (due to the typical spectral shape of Bremsstrahlung emerging from the primary electrons). Further details regarding the data evaluation were described earlier [9].

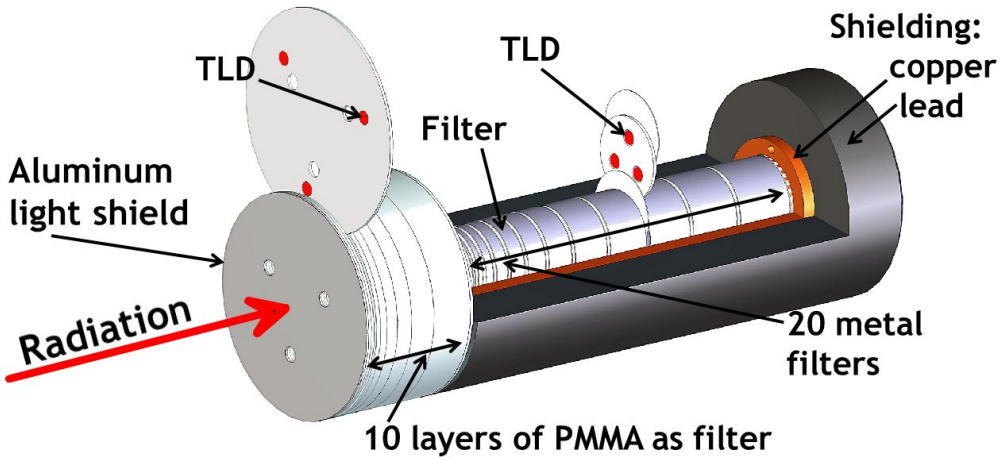

Figure 2. Sketch of the TLD-based spectrometer. Basic principle: the deeper the radiation penetrates, the higher its energy.

3.2 Measurements with the FCS

The FCS was located inside the target chamber with its front face at 0.2 m distance from the laser target and directed to the laser focus point on the target wire, see figure 1. In total, the FCS was irradiated with 13 laser shots at a mean laser energy of (29 ± 4) J, see table 2. Figure 3 shows the experimental setup inside the target chamber. Using the data evaluation described in the previous subsection, the absolute fluence at the front face of the FCS was determined for both contributions electrons and photons: $\Phi_{0.2\mathrm{m;FCS;el}}$ and $\Phi_{0.2\mathrm{m;FCS;ph}}$.

2022 JINST 17 P05033

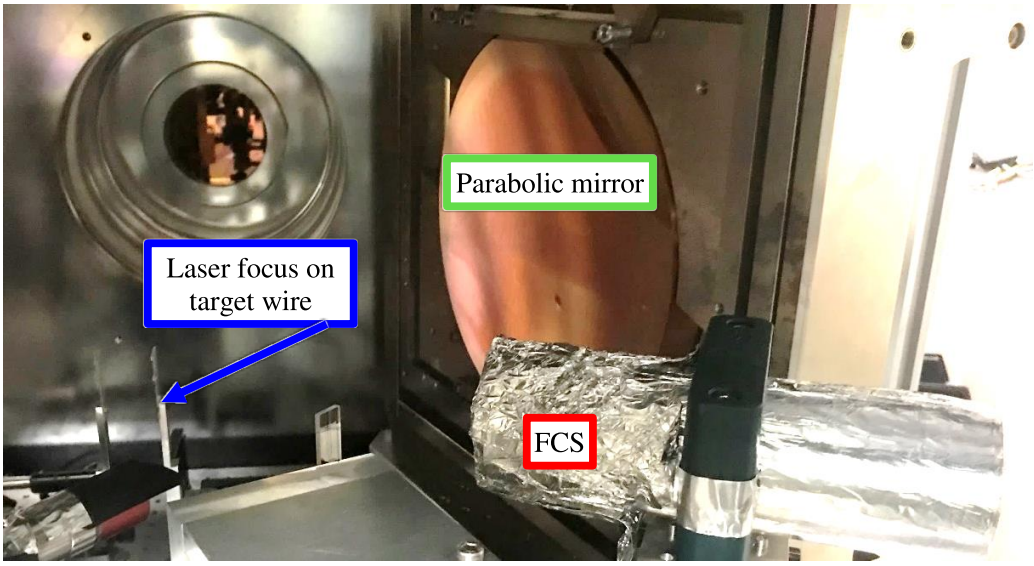

Figure 3. Experimental setup inside the target chamber with the parabolic mirror (green) to focus the laser beam on the target wire (blue) and the FCS facing the laser focus. The laser beam impinges from the left onto the parabolic mirror.

4 Particle transport simulations from inside to outside of the target chamber

4.1 The EGSnrc software and chosen transport parameters

From the absolute spectra measured inside the target chamber using the FCS, the dose and the particle spectra outside the target chamber were calculated using the Monte Carlo particle transport code package EGSnrc [21]. For the calculation of the dose and spectra the user codes DosRZnrc and FluRZnrc, respectively, were used. Among others, with these two user codes, it is rather simple to define cylindrical geometries and they come with the installation of EGSnrc. The following main transport parameters were chosen: the cross-sectional data for the electron transport (where the condensed history technique is applied) are: standard EGSnrc (based on the Bethe-Bloch theory) for collision stopping power and Bethe-Heitler cross sections for radiative stopping power. For photons, the XCOM cross sections are used. The maximum energy loss per electron step is 25 % (ESTEPE = 0.25) and photons and electrons are followed down to an (kinetic) energy of 10 keV. Furthermore, exact boundary crossing, PRESTA-II, active spin effects and electron impart ionization, bound Compton scattering, photoelectron angular sampling, Rayleigh scattering, and atomic relaxations were activated. Finally, to obtain better statistics of the resulting photon spectra originating from the primary electrons, bremsstrahlung splitting was activated using FluRZnrc with 50 photons (each with a weight of 1/50).

4.2 Geometry and simulations performed with EGSnrc

4.2.1 Calculation of the dose using DosRZnrc

The user code DosRZnrc of the EGSnrc code package together with the absolute fluence spectra from the FCS as input, $\Phi_{0.2\mathrm{m;FCS}}$, was used to calculate the dose outside the target chamber at the position of the Dosepix dosemeter, i.e., at a distance of 3.67 m from the target wire. The Dosepix dosemeter

2022 JINST 17 P05033

is intended to measure the operational quantity personal dose equivalent, $H_p(10)$, being defined at 10 mm depth in a phantom made of ICRU 4-element tissue [22]. Accordingly, the dose was calculated at 10 mm depth in a phantom made of ICRU 4-element tissue, $H_p(10)_{3.67m;DosRZnrc}$. For both contributions, the electron and photon fluence spectra measured with the FCS, $\Phi_{0.2m;FCS;el}$ and $\Phi_{0.2m;FCS;ph}$, separate simulations were performed, and the corresponding doses, $H_p(10)_{3.67m;DosRZnrc;el}$ and $H_p(10)_{3.67m;DosRZnrc;ph}$, were summed up to the total dose, $H_p(10)_{3.67m;DosRZnrc}$. The geometry including the geometrical details of the simulations is shown in figure 4. A point source positioned at the position of the target wire with a beam diameter of 80 cm at the front face of the FCS, i.e., 20 cm from the target wire, was used with $\Phi_{0.2m;FCS;el}$ and $\Phi_{0.2m;FCS;ph}$ as the two inputs.

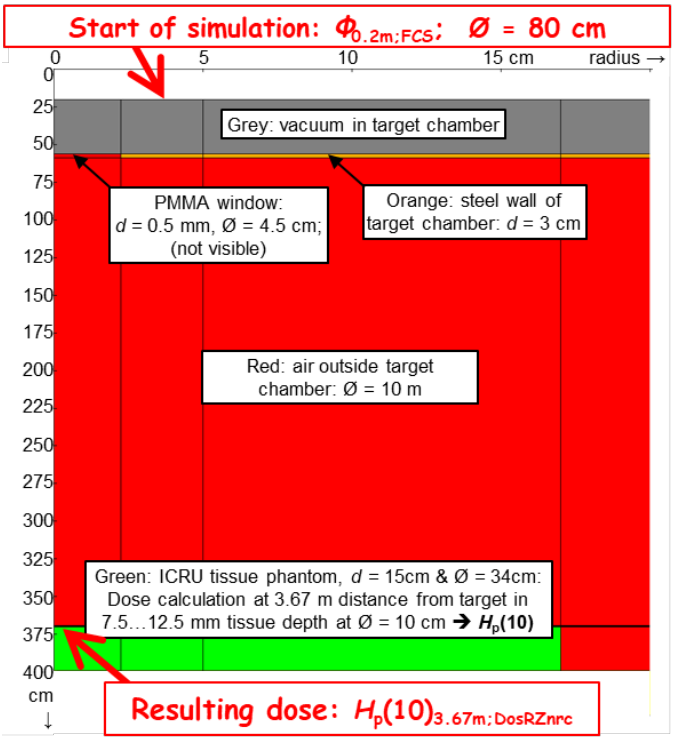

Figure 4. Geometry of the simulations using the DosRZnrc user code. The left side represents the geometry's rotational axis; the vertical lines indicate the radial region boundaries (radius given at the top) and the horizontal lines indicate the region boundaries perpendicular to the rotational axis (distance from the origin given at the left). Different colors represent different materials, see descriptions in the figure (PMMA being polymethyl methacrylate). The figure was created using the EGSnrc package based on the input file for the simulations, the small numbers give the coordinates in cm (top: radial distance from the target wire; left: distance from the target wire).

4.2.2 Calculation of the particle spectra using FluRZnrc

Similar to the dose calculations described above, the particle fluences at a distance of 3.67 m from the target wire, i.e., also at the position of the Dosepix dosemeter, were calculated using the EGSnrc user code FluRZnrc. The geometry is rather the same as shown in figure 4 except that the tissue phantom was replaced by vacuum in order to obtain only the fluence impinging on the Dosepix dosemeter from its front. Again, separate simulations were performed for the electron and photon contributions

2022 JINST 17 P05033

measured with the FCS. Two fluence contributions resulted from each simulation, i.e., two electron and two photon fluence contributions at 3.67 m. From the corresponding two contributions both the total electron and photon fluence were summed up resulting to $\Phi_{3.67\text{m;FluRZnrc;el}}$ and $\Phi_{3.67\text{m;FluRZnrc;ph}}$, see figure 5.

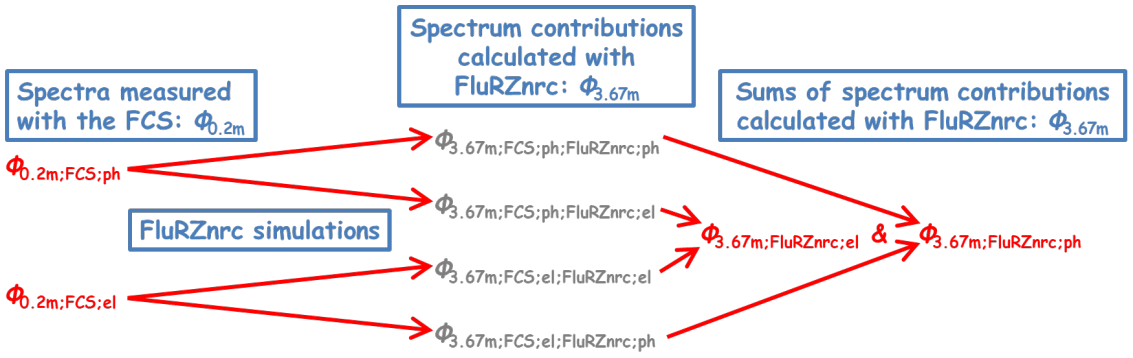

Figure 5. Illustration of the calculations using FluRZnrc to obtain the spectra outside the target chamber at 3.67 m distance from the target wire.

4.3 Validation of the simulations

A validation of the simulations, i.e., of the use of EGSnrc to define the geometry and its further input settings used, was performed by comparing the dose calculated by DosRZnrc, $H_\text{p}(10)_{3.67\text{m;DosRZnrc}}$, with the dose determined from the particle spectra, $\Phi_{3.67\text{m;FluRZnrc}}$, calculated by FluRZnrc: $H_\text{p}(10)_{3.67\text{m;FluRZnrc}}$. The latter was calculated by the following equation: $H_\text{p}(10)_{3.67\text{m;FluRZnrc}} = \{\Phi_{3.67\text{m;FluRZnrc;el}} \cdot h_{\text{p}\Phi}(10)_\text{el}\} + \{\Phi_{3.67\text{m;FluRZnrc;ph}} \cdot h_{\text{p}\Phi}(10)_\text{ph}\}$ with $h_{\text{p}\Phi}(10)_\text{el}$ and $h_{\text{p}\Phi}(10)_\text{ph} = \{K_a/\Phi\}_\text{ph} \cdot h_{\text{p}K}(10)_\text{ph}$ the conversion coefficient from particle fluence to $H_\text{p}(10)$ for electrons and photons, respectively, and with $\{K_a/\Phi\}_\text{ph}$ the kerma factor and $h_{\text{p}K}(10)_\text{ph}$ the conversion coefficient from air kerma to $H_\text{p}(10)$, the two latter for photons. The values for $h_{\text{p}\Phi}(10)_\text{el}$ and $h_{\text{p}K}(10)_\text{ph}$ were taken from ICRU 57 [23] while for particle energies above 10 MeV for $h_{\text{p}\Phi}(10)_\text{el}$ and $h_{\text{p}K}(10)_\text{ph}$ the same value as given for 10 MeV was used as ICRU 57 does only contain data up to 10 MeV. The values for $\{K_a/\Phi\}_\text{ph}$ were taken from NISTIR [24].

5 Measurements outside the target chamber

5.1 Detectors

5.1.1 The Dosepix dosemeter

For the measurements outside the PHELIX target chamber firstly, a Dosepix dosemeter consisting of three Dosepix detectors was used. The Dosepix detectors are hybrid, photon counting pixel ASICs developed in a cooperation between the Erlangen Center for Astroparticle Physics (ECAP) and CERN [12]. The Dosepix detector was designed for applications in dosimetry [13]. The pixel matrix of the Dosepix comprises 16×16 pixels at a pitch of 220 µm. Each of the 256-pixel cell circuitries features a charge sensitive preamplifier connected to a leading-edge discriminator. The length of the digital output of the discriminator - which is correlated with the deposited energy - is named

2022 JINST 17 P05033

time-over-threshold (ToT). For each event, the ToT is determined in a 12-bit ToT binary counter by counting clock cycles. Besides a fast energy histogramming mode, which sorts each event in one of the 16 energy channels in the hit pixel according to the ToT, the Dosepix features other operation modes such as the ToT-integration mode. The integration mode mimics a charge integrating detector by summing the ToT of successive events in each pixel. During readout, the integrated ToT values are transferred to the periphery for each pixel. For the study presented here, the Dosepix was operated in the integration mode. This Dosepix was bump-bonded pixelwise to a 300 µm thick p-in-n silicon sensor as radiation sensitive layer. By adequate doping of a guard ring structure on the backside of the sensor, 4×16 pixels with 55 µm × 55 µm and 12×16 pixels with 220 µm × 220 µm front area were realized in the 300 µm thick sensor. The small pixels have an active volume reduced by a factor 16 compared to the large pixels in order to increase the dynamical range for measurements. The data evaluation used is based on a neural network which has been trained and validated earlier. The feedforward neural network used for regression was trained with simulated photon spectra. The simulated detector response used as input for the network was obtained from the simulated energy response of the three Dosepix detectors irradiated with monoenergetic photons [25] , i.e., the signal in the three detectors per incident photon fluence. The corresponding output of the neural network denotes the personal dose equivalents $H_{\mathrm{p}}(10)$ and $H_{\mathrm{p}}(0.07)$ that can be calculated, as described above, from the photon fluence by multiplication with the corresponding conversion coefficients [23]. 90 % of more than 100000 simulated spectra were used for training and the remaining 10 % for validation of the neural network.

5.1.2 The PIN diodes

Secondly, the use of two Hamamatsu 3590-19 PIN diodes in the extreme radiation field was investigated. They consist of Silicon wafers, 300 µm in thickness with a 10 mm × 10 mm cross sectional area positioned in a housing made of Aluminum (Al). The first diode was covered with 30 µm Al and the second one with 30 µm Al and 50 µm Copper (Cu). Both diodes were operated at 85 V and as signal their charge per laser shot was collected. The induced charge was directly measured by a LeCroy Wx104 oscilloscope with analogue bandwidth of 1 GHz.

5.1.3 The Timepix detector

Thirdly, the use of the Timepix detector was investigated. Similar to Dosepix, Timepix is a hybrid, pixelated, photon-counting X-ray detector developed by the Medipix collaboration with its seat at CERN. In our case 256×256 Cadmium-Telluride (CdTe) pixels are bump-bonded to form sensor pixels of 55 µm × 55 µm area (resulting in a sensitive area of approximately 14 mm × 14 mm) with a thickness 1000 µm. In contrast to the frame-based readout of Dosepix, Timepix3 is operated in a data driven operation mode: each pixel having experienced a hit above threshold sends event data out to the readout after the signal drops below the threshold again. The event data consists of the pixel coordinates in the pixel matrix, a fine and a coarse time stamp and the Time over Threshold (ToT, with a 10-bit resolution). The latter is taken as measure for the deposited energy. The CdTe-sensor layer of the Timepix detector was biased with −300 V so that the pixel electrodes collect the electrons released by the ionizing particles in the CdTe sensor layer. The Timepix was shielded by sufficient lead to reduce the overlay probability of induced radiation events to enable the separation and counting of these events during a radiation pulse, i.e., to prevent pile-up effects.

2022 JINST 17 P05033

For the data analysis, the number of pixels hit caused by a radiation burst was investigated. Further details regarding the Timepix and its data evaluation can be found in the literature [14].

5.2 Measurements

5.2.1 Measurements with the Dosepix dosemeter

The Dosepix dosemeter was positioned in the direction of a window in the target chamber made of 0.5 mm polymethyl methacrylate (PMMA) at 3.67 m from the target wire (figure 1). It is mounted on an ISO water slab phantom [26] to mimic the backscattered radiation that were present if the dosemeter were placed on a human trunk. In total, the Dosepix dosemeter was irradiated with 15 laser shots at a mean laser energy of (23 ± 3) J (table 2(a)). Figure 6 shows its experimental setup outside the target chamber. Using the data evaluation described in the previous subsection, the absolute dose at the position of the Dosepix dosemeter was determined: $H_{\mathrm{p}}(10)_{3.67\mathrm{m;Dosepix}}$.

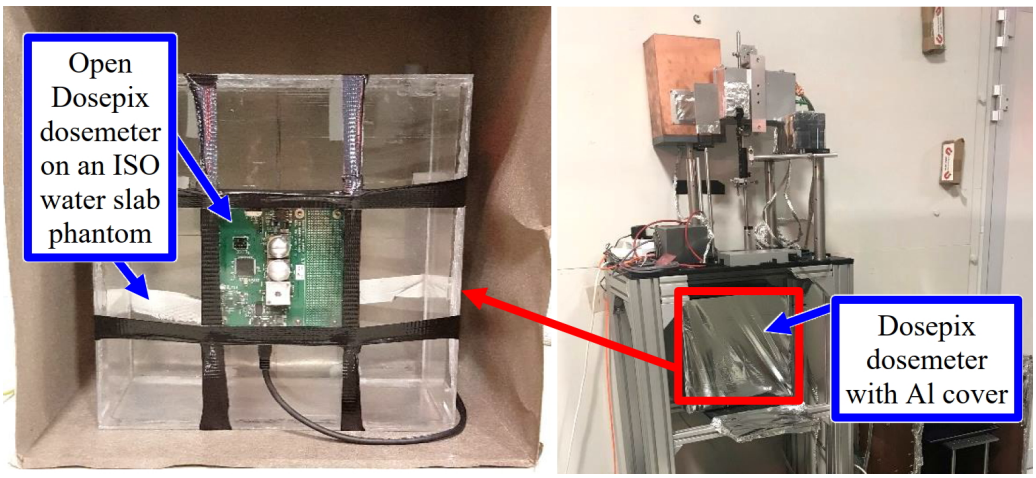

Figure 6. Dosepix dosemeter in detail (left) and positioned outside the target chamber (right, hidden behind an Aluminum foil).

5.2.2 Measurements with the PIN diodes

As with the Dosepix dosemeter, the PIN diodes were positioned in the direction of a 0.5 mm PMMA window in the target chamber at a distance of 1.75 m from the target wire (see figure 1). In total, the diodes were irradiated with 3 laser shots at laser energies ranging from 20.0 J up to 31.0 J., further details regarding the experimental setup are given in table 2(b). Figure 7 shows the experimental setup outside the target chamber.

5.2.3 Measurements with the Timepix detector

Similar to the other detectors, the Timepix was positioned facing the direction of a 0.5 mm PMMA window in the target chamber at a distance of 3.67 m from the target wire (see figure 1). In total, the Timepix was irradiated with 4 laser shots at laser energies ranging from 21.6 J up to 32.3 J, further details regarding the experimental setup are given in table 2(b). Figure 8 shows the experimental setup outside the target chamber.

2022 JINST 17 P05033

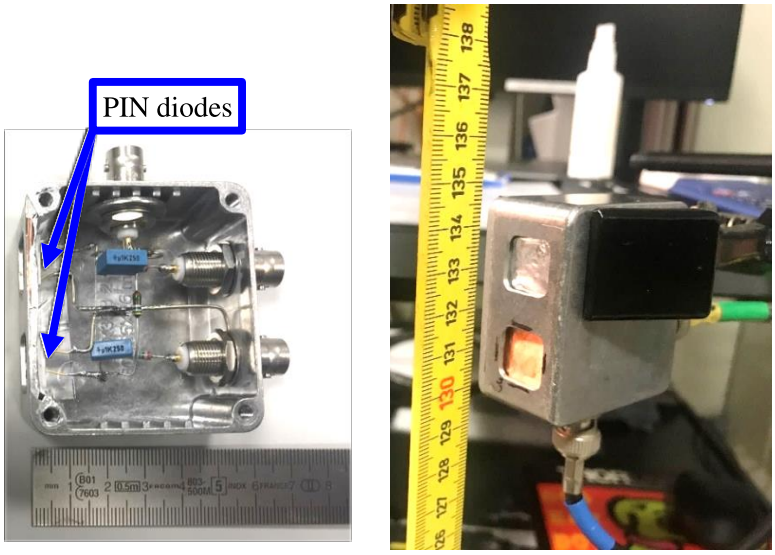

Figure 7. PIN diodes in their open housing showing, besides the diodes themselves, electronic components (left) and their closed housing with the entrance windows outside the target chamber (right).

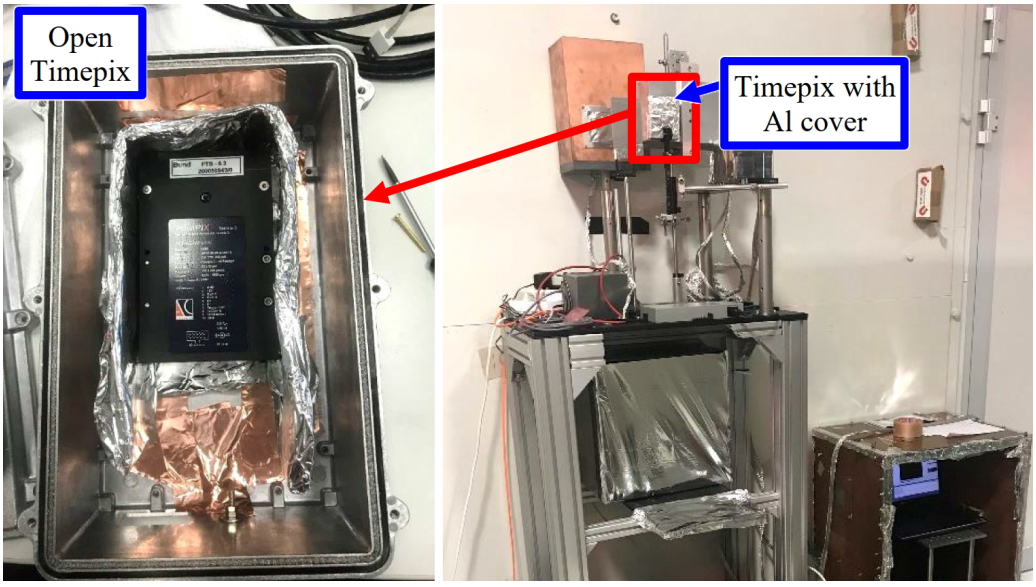

Figure 8. Timepix detector in detail (left) outside the target chamber (right).

6 Results

6.1 FCS-measured electron and photon spectra inside the target chamber

Figure 9 shows the absolute electron and photon spectra per laser shot (averaged over the 13 laser shots with the FCS with (29 ± 4) Joule laser energy per shot (standard deviation of the single values, $k = 1$), see table 1 and table 2 for further details during the experiments). The uncertainty bars denote the standard uncertainties ($k = 1$) due to the statistical fluctuations of the simulation, i.e., type A uncertainties. The type B uncertainties with the main contribution from the interaction

2022 JINST 17 P05033

coefficients of the simulation are estimated to be in the order of 5 % and 3 % for electrons and photons, respectively. For electrons, the two contributions of the Maxwellian distribution show rather different slopes (represented by the Boltzmann temperature of the plasma) indicating two plasma contributions with different hot electron temperatures. As the photons emerge from the electrons in the plasma (by Bremsstrahlung production), their slopes show a similar behavior.

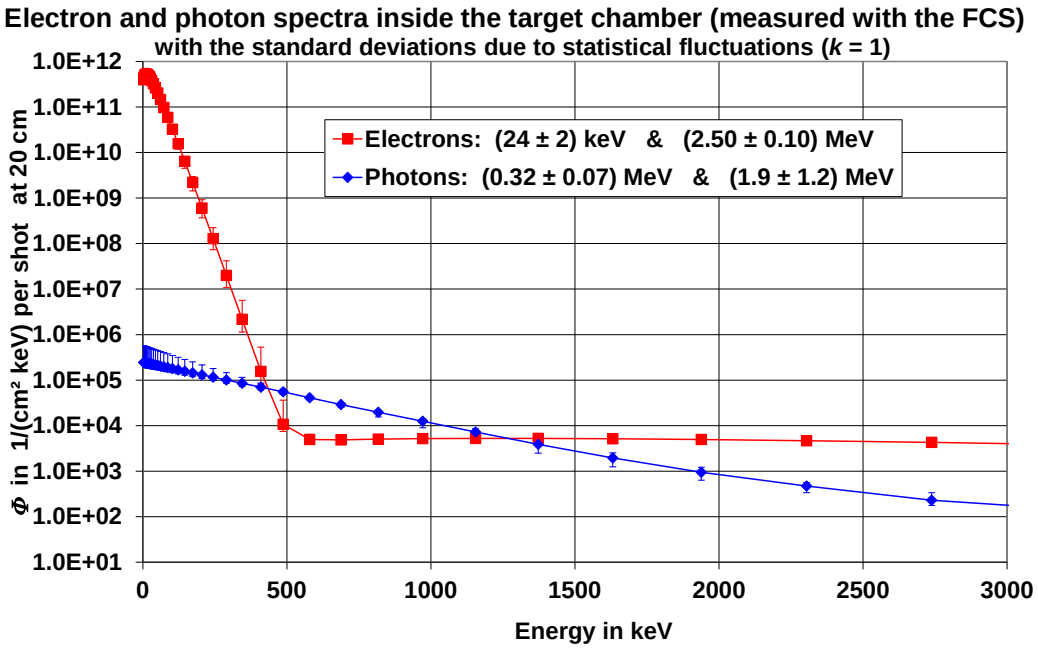

Figure 9. Electron and photon spectra per laser shot at 0.2 m distance from the target wire measured inside the target chamber with the FCS. The legends give the Boltzmann temperature and slope of the Maxwellian distributions (for electrons) and exponential decreases (for photons), respectively, together with their standard uncertainties ($k = 1$).

6.2 EGSnrc-simulated doses and particle spectra outside the target chamber

6.2.1 Dose values from the DosRZnrc simulations

The dose values outside the target chamber at the measurement position of the Dosepix dosemeter were calculated as described in subsection 4.2.1 from the FCS-measured spectra. The electron and photon contribution per laser shot is (2.25 ± 0.20) µSv/shot and (0.54 ± 0.02) µSv/shot, respectively, resulting to a total dose of $H_p(10) = (2.79 \pm 0.21)$ µSv/shot. The uncertainties given are the total standard uncertainties, $k = 1$. They combine the statistical fluctuations of the simulation, i.e., the type A uncertainties, and the type B uncertainties with the main contribution from the interaction coefficients of the simulation which are estimated to be in the order of 5 % and 3 % for electrons and photons, respectively.

6.2.2 Spectra from the FluRZnrc simulations

Also, from the FCS-measured spectra, the particle spectra at the measurement position of the Dosepix dosemeter were calculated as described in subsection 4.2.2. The ordinate in figure 9 covers eleven

2022 JINST 17 P05033

orders of magnitude for the spectra measured at 0.2 m distance inside the target chamber. Likewise, the ordinate of figure 10 also covers eleven orders of magnitude (only at smaller values) for the resulting spectra at 3.67 m distance outside the target chamber. Since both axes cover the same number of orders of magnitude a rather simple comparison of the two sets of spectra is possible. The distance of the Dosepix dosemeter compared to the FCS is much larger, i.e., 0.2 m compared to 3.67 m from the target wire. Furthermore, the radiation undergoes significant scattering and absorption effects on the way from the FCS to Dosepix dosemeter's positions, especially the electrons. Therefore, the spectra at the Dosepix dosemeter's position are several orders of magnitude smaller compared to the spectra at the FCS position while the shapes of the spectra are rather similar, see figure 10 in contrast to figure 9. The significant electron absorption is obvious as the many low energy electrons at the FCS position below about 500 keV energy have completely disappeared at the Dosepix dosemeter's position. The extreme fluctuations of the electron fluence at energies below about 200 keV originates from the rather large uncertainties of more than 90 % of the contribution due to primary electrons, although the CPU simulation time has been several weeks on a computer cluster.

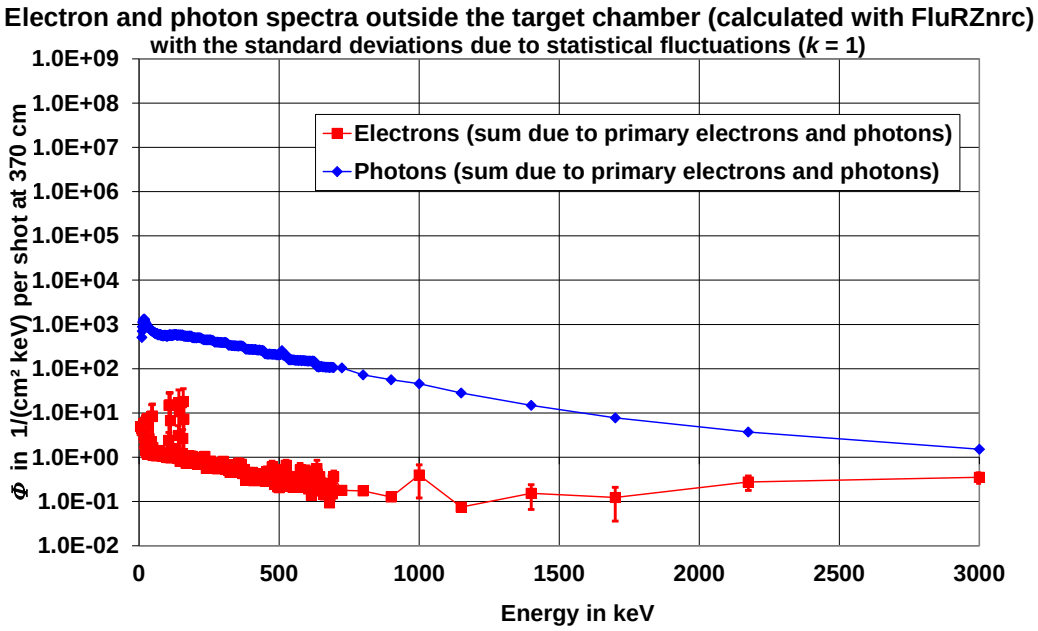

Figure 10. Electron and photon spectra per laser shot at 3.67 m distance from the target wire calculated for outside the target chamber with FluRZnrc. As in figure 9, the ordinate covers eleven orders of magnitudes to provide a rather simple comparison of the two sets of spectra.

6.2.3 Validation of the simulations

Table 3 shows dose values calculated using DosRZnrc in comparison to those determined from the spectra calculated using FluRZnrc and the conversion coefficients from particle fluence to dose (see subsection 4.3). Both dose contributions due to primary photons and electrons as well as the total doses agree within the uncertainties. Therefore, the two simulation methods are considered to be correctly implemented in the simulation software EGSnrc.

2022 JINST 17 P05033

Table 3. Comparison of dose values, $H_p(10)$, from the simulations using DosRZnrc and FluRZnrc, together with their total uncertainties ($k = 1$) due to the statistical fluctuations of the simulation, i.e., type A uncertainties, and the type B uncertainties of the simulation (with the main contribution assumed to be from the interaction coefficients in the order of 5 % and 3 % for electrons and photons, respectively).

Particle type	DosRZnrc µSv/shot	FluRZnrc µSv/shot
Dose due to primary electrons	$H_p(10)_{3.67m;el;DosRZnrc}$ 2.25 ± 0.20	$H_p(10)_{3.67m;el;FluRZnrc}$ 2.27 ± 0.18
Dose due to primary photons	$H_p(10)_{3.67m;ph;DosRZnrc}$ 0.54 ± 0.02	$H_p(10)_{3.67m;ph;FluRZnrc}$ 0.56 ± 0.02
Total dose	$H_p(10)_{3.67m;el\&ph;DosRZnrc}$ 2.79 ± 0.21	$H_p(10)_{3.67m;el\&ph;FluRZnrc}$ 2.83 ± 0.18

For further information, table 4 shows the separate dose contributions to the total dose, $H_p(10)$, based on the simulations using FluRZnrc. The method for the determination of the four contributions is illustrated above in figure 5. Obviously, the electron contribution due to the primary electrons measured with the FCS is the most dominant part with approximately 75 % while the electron contribution due to the primary photons measured with the FCS is negligible. From this, two main points are concluded. Firstly, a significant number of primary electrons reach the Dosepix dosemeter's position and secondly, the energetic primary electrons produce a lot of Bremsstrahlung on their way from the inside to the outside of the target chamber, probably in the target chamber wall which is made of 3 cm steel (see figure 4), which, in turn, produce secondary electrons on their way to the Dosepix dosemeter's position, being energetic enough to contribute to $H_p(10)$.

Table 4. Contributions to the dose, $H_p(10)$, from the simulations using FluRZnrc, together with their total uncertainties ($k = 1$), for details regarding the uncertainty, see caption of table 3. In comparison to table 3, the indices were extended in the end to consider the corresponding dose contribution.

Particle type	Electron contribution to dose µSv/shot	Photon contribution to dose µSv/shot
Dose due to primary electrons	$H_p(10)_{3.67m;el;DosRZnrc;el}$ 2.16 ± 0.18	$H_p(10)_{3.67m;el;FluRZnrc;ph}$ 0.11 ± 0.01
Dose due to primary photons	$H_p(10)_{3.67m;ph;DosRZnrc;el}$ < 0.01	$H_p(10)_{3.67m;ph;FluRZnrc;ph}$ 0.55 ± 0.02
Dose due to primary electrons and primary photons	$H_p(10)_{3.67m;el\&ph;DosRZnrc;el}$ 2.17 ± 0.18	$H_p(10)_{3.67m;el\&ph;FluRZnrc;ph}$ 0.66 ± 0.02
Total dose	$H_p(10)_{3.67m;el\&ph;FluRZnrc;el\&ph}$ 2.83 ± 0.18	

6.3 Dosepix-measured doses outside the target chamber

Figure 11 shows the doses per laser shot measured with the Dosepix dosemeter depending on the laser energy per shot (see table 1 and table 2(a) for further details during the experiments). For the

2022 JINST 17 P05033

10 µm target wire, the (nearly) linear correlation leads to the assumption that no significant pile-up or other effects, negatively affect the measurement and subsequent data evaluation of the Dosepix dosemeter while the correlation is much poorer for the 5 µm target wire, as can be seen in figure 11 where the uncertainties of the fit parameters are larger than 100 % for the 5 µm target wire. The strong fluctuation of the data points is probably attributed to the rather large uncertainties of the measurements (which might have been influenced by the presence of high-frequency electromagnetic disturbances in the experimental hall) and larger for the 5 µm target wire, probably because the signals and resulting doses are smaller. Finally, it is important to note that the neural network used for the data evaluation has only been trained in photon radiation fields (see subsection 5.1.1). In the PHELIX radiation field however, the dominant contribution originates from electrons according to the simulation results above (see table 3 and table 4). Anyway, the results are considered to be valid for the following reason: like in electron radiation fields, also in photon fields (used for the training of the neural network), any detector signal origins from secondary electrons which are directly ionizing while photons are not (ionization due to photons always origins from secondary electrons produced in the detector and its surrounding material). To make sure the results in the mixed electron photon fields are really reliable, future Dosepix dosemeter measurements in well-defined electron radiation fields are planned to confirm that the algorithm of the neural network is also suitable for electron radiation fields and, with this, for the measurements at the PHELIX facility. Due to the facts mentioned above, the non-statistical contributions to the uncertainties (type B) of the Dosepix results are estimated to be rather large, i.e., larger than several tens of percent. The uncertainties due to statistical fluctuations can be seen in the fluctuation of the values shown in figure 11. From these fluctuations, the uncertainties of the resulting fit parameters were deduced.

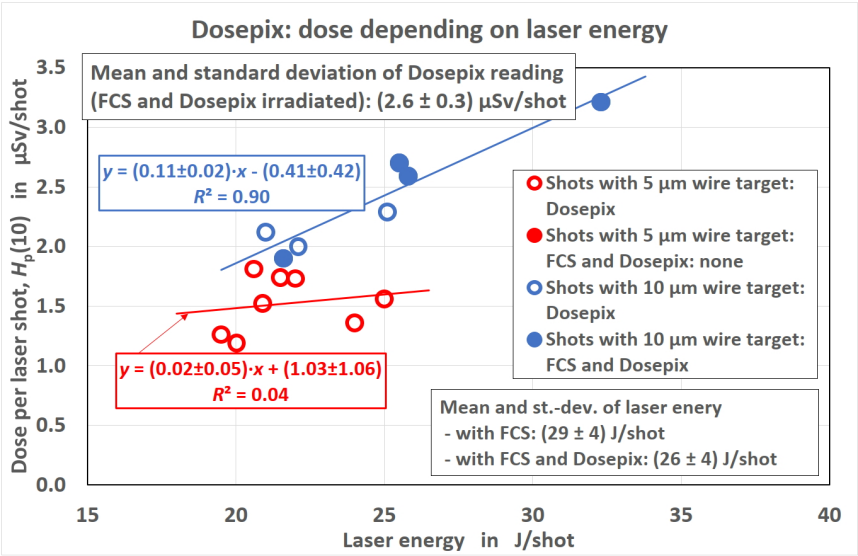

Figure 11. Dose values, $H_p(10)$, per laser shot measured with the Dosepix dosemeter depending on the laser energy per shot. Symbols: measured values; lines: linear regressions of the measured values; open symbols Dosepix dosemeter while the FCS was not present; closed symbols Dosepix dosemeter while also the FCS was present. The uncertainties stated in the boxes are standard uncertainties (for the fit parameters), standard uncertainties of the mean (for the dose per shot) and of the single values (for the laser energies per shot) ($k = 1$) due to the statistical fluctuations of the single values, i.e., type A uncertainties.

2022 JINST 17 P05033

6.4 PIN diodes-measured doses outside the target chamber

Figure 12 shows the charge collected in the two PIN diodes (behind the Al filter and behind the Al&Cu filter, for details see subsection 5.2.2) per laser shot depending on the laser energy per shot (see table 1 and table 2(b) for further details during the experiments). The linear correlations (due to the smaller signal much poorer for the diode behind the AL&Cu cover) of the (only three data points for each diode), hint that these detectors also show no significant pile-up or other effects negatively affecting the measurement although they might also be affected by the presence of high-frequency electromagnetic disturbances in the experimental hall. Furthermore, the extrapolations show that a minimum laser energy of approximately 18 J seems to have been necessary to produce enough radiation to be detected in the diodes (see figure 12). In summary, it is concluded that the PIN diodes are, in principle, suitable for measurements in extreme radiation fields such as that present at the PHELIX facility, although their quantitative suitability needs to be proven by further experiments.

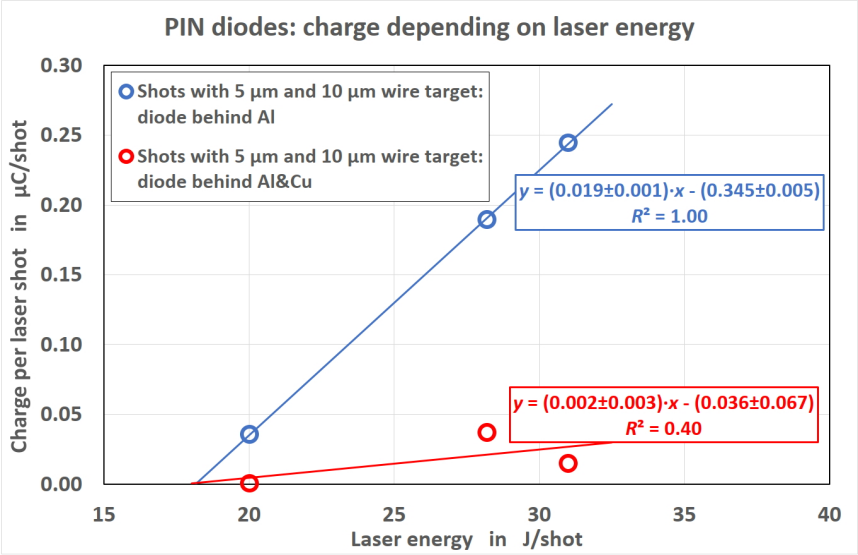

Figure 12. Charge per laser shot measured with the PIN diodes behind the different filters, see legend, depending on the laser energy per shot. Symbols: measured values; lines: linear regressions of the measured values. The fit parameters are given with their standard uncertainties while the uncertainties of the single charge values can, unfortunately, not yet estimated as the experiments only serve as a first test.

6.5 Timepix-measured doses outside the target chamber

Figure 13 shows the number of pixels hit by radiation (for details see subsection 5.2.3), per laser shot depending on the laser energy per shot (see table 1 and table 2(b) for further details during the experiments). The linear correlation of, unfortunately only four data points, suggests that this detector also shows no significant pile-up or other effects, negatively affecting the measurement. Furthermore, the linear function from the fit of the number of triggered pixels as function of laser energy has an intersection with the ordinate at about 5200 pixels (however, with a rather large uncertainty of more than 100 % as calculated by the linear regression, see figure 13). One explanation for this could be the presence of high-frequency electromagnetic disturbances in the experimental hall that occur during the laser pulse that might trigger pixels. Due to the very small number of

2022 JINST 17 P05033

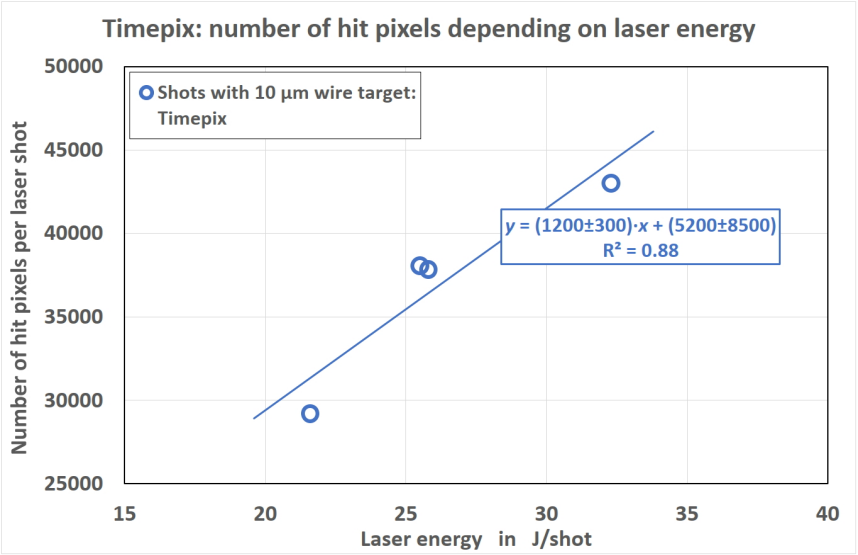

Figure 13. Number of hit pixels per laser shot measured with the Timepix depending on the laser energy per shot. Symbols: measured values; lines: linear regressions of the measured values. The uncertainties can, unfortunately, not yet estimated as the experiments only serve as a first test.

four data points, the experiments performed using the Timepix can only be taken as a first hint for assuming that it is suitable for measurements in extreme radiation fields such as those present at the PHELIX facility — which needs to be proven by further experiments.

6.6 Comparison of results

The FCS and the Dosepix dosemeter were irradiated simultaneously during 4 laser shots. In total, the FCS collected the dose during 13 laser shots to provide large enough signals in the TLDs for their read out. Consequently, the results presented in subsection 6.1 are valid for the mean of these 13 laser shots during which two different target wires and with slightly varying laser energies were used (see table 2(a) and figure 11). In contrast to the FCS, the Dosepix dosemeter is an active device and the signals during each laser shot were evaluated separately. Therefore, for comparing the FCS and Dosepix dosemeter results, the dose values deduced from the spectra measured with the FCS (irradiated during 13 laser shots) can only be compared to the dose values measured with the Dosepix dosemeter during the 4 common laser shots. Anyway, this comparison is considered valid as the parameters during these two sets of experiments (13 shots of FCS of which 4 shots were together with the Dosepix dosemeter) are rather similar (again, see table 2(a)).

The FCS spectra measured at 0.2 m distance from the target wire inside the target chamber, in combination with the particle transport simulations using EGSnrc, result in a total dose at 3.67 m distance from the target wire outside the target chamber of (2.8 ± 0.2) µSv/shot (average over 13 laser shots with the FCS with estimated total uncertainty). In comparison, the measurements with the Dosepix dosemeter result in a dose of (2.6 ± 0.3) µSv/shot (average over the 4 laser shots with the FCS and Dosepix together with standard uncertainty of the mean). Thus, the two totally independent methods to derive the dose at the measurement position of the Dosepix dosemeter lead to the same results within their standard uncertainties confirming all three: i) the measurement and data evaluation

2022 JINST 17 P05033

of the FCS, ii) the simulations undertaken using EGSnrc, and finally, iii) the measurement and data evaluation of the Dosepix dosemeter. However, this conclusion is only preliminary as the suitability of the neural network algorithm used for the electron dominated radiation field needs to be confirmed by further measurements and data evaluations of the Dosepix dosemeter in well-defined electron radiation fields (see subsection 5.1.1). For this, measurements at an irradiation facility for beta-particle reference radiation fields at PTB are planned, i.e., at the Beta Secondary Standard 2, BSS 2 [27, 28].

7 Conclusions

In this work, two totally different methods to measure the ionizing radiation emission from a Tungsten target irradiated by the PHELIX laser facility at GSI yielded comparable dose results, i.e., a passive device (FCS) measuring the particle spectra inside the PHELIX target chamber and an active device (Dosepix dosemeter) measuring the dose outside the PHELIX target chamber. For the comparison of these two different measurements, simulations were performed using the Monte Carlo particle transport code package EGSnrc to obtain from the spectra inside the target chamber the dose outside. As the two differently obtained dose values agree within their uncertainties, it seems that all three parts, the two measurement methods and the simulations, are reliable. However, this needs to be confirmed by future measurements.

Furthermore, two additional devices for radiation measurements were used: two active detectors (PIN diodes and Timepix) measuring outside the PHELIX target chamber. Also, the results of these two devices give good hints that they are suitable for measurements in such extreme radiation fields (ultra-short pulses of mixed photon and electron radiation) as their signal correlates with the laser energy per shot. Anyway, this needs to be confirmed by future investigations.

Acknowledgments

The authors would like to thank Paul Neumayer and Bernhard Zielbauer together with the whole PHELIX-team (GSI Darmstadt) for their indispensable support during the experiments, Phil Brüggemann (PTB Braunschweig) for the packing and unpacking of the FCS and for performing the read out of the several hundreds of TLDs, Gert Lindner (PTB Berlin) for his permanent support when using the high-performance compute cluster (HPC) of PTB on which the simulations were carried out and George Winterbottom (PTB Braunschweig) for checking over the manuscript.

Funding. This work was funded by the Deutsche Forschungsgemeinschaft (DFG — German Research Foundation) under Grant HU 2660/1-1 — 394324524 and MI 1507/4-1-643633.

References

[1] C. Gerhard, W. Viöl and S. Wieneke, *Plasma-enhanced laser materials processing*, in *Plasma Science and Technology — Progress in Physical States and Chemical Reactions*, InTech (2016), https://doi.org/10.5772/61567.

[2] O. Hupe, H. Zutz and J. Klammer, *Radiation protection dosimetry in pulsed radiation fields*, presented at *IRPA 13* Glasgow, U.K., 14–18 May 2021, contribution TS2f.3 [presentation: https://www.irpa.net/members/1130%20thu%20alsh%20Hupe%20TS2f.3.pdf] [full paper: https://www.irpa.net/members/TS2f.3.pdf].

2022 JINST 17 P05033

[3] R. Hanke, T. Fuchs and N. Uhlmann, *X-ray based methods for non-destructive testing and material characterization*, *Nucl. Instrum. Meth. A* **591** (2008) 14.

[4] T.C. Zhu and K.K.-H. Wang, *Linear accelerators (LINAC)*, in *Encyclopedia of Radiation Oncology*, L-M. Brady and T.E. Yaeger, eds., pp. 437–450, Springer Berlin Heidelberg (2013), https://doi.org/10.1007/978-3-540-85516-3_37.

[5] L. Labate, D. Palla, D. Panetta, F. Avella, F. Baffigi, F. Brandi et al., *Toward an effective use of laser-driven very high energy electrons for radiotherapy: Feasibility assessment of multi-field and intensity modulation irradiation schemes*, *Sci. Rep.* **10** (2020) 17307.

[6] U. Ankerhold, O. Hupe and P. Ambrosi, *Deficiencies of active electronic radiation protection dosemeters in pulsed fields*, *Radiation Protection Dosimetry* **135** (2009) 149.

[7] R. Behrens and P. Ambrosi, *A TLD-based few-channel spectrometer for mixed photon, electron, and ion fields with high fluence rates*, *Radiat. Prot. Dosim.* **101** (2002) 73.

[8] R. Behrens, *A spectrometer for pulsed and continuous photon radiation*, 2009 *JINST* **4** P03027.

[9] R. Behrens, H. Schwoerer, S. Düsterer, P. Ambrosi, G. Pretzler, S. Karsch et al., *A thermoluminescence detector-based few-channel spectrometer for simultaneous detection of electrons and photons from relativistic laser-produced plasmas*, *Rev. Sci. Instrum.* **74** (2003) 961.

[10] R. Behrens, B. Pullner and M. Reginatto, *Measurements at laser materials processing machines: spectrum deconvolution including uncertainties and model selection*, *J. Sensors Sensor Syst.* **10** (2021) 13.

[11] R. Behrens, H. Zutz and J. Busse, *Spectrometry of pulsed photon radiation*, *J. Radiol. Prot.* **42** (2022) 011507.

[12] W. Wong, G. Anton, R. Ballabriga, M. Böhnel, M. Campbell, E. Heijne et al., *A pixel detector asic for dosimetry using time-over-threshold energy measurements*, *Radiat. Meas.* **46** (2011) 1619.

[13] D. Haag, S. Schmidt, P. Hufschmidt, F. Eberle, T. Michel, G. Anton et al., *Personal dosimetry in continuous photon radiation fields with the dosepix detector*, *IEEE Trans. Nucl. Sci.* **68** (2021) 1129.

[14] T. Poikela et al., *Timepix3: a 65K channel hybrid pixel readout chip with simultaneous ToA/ToT and sparse readout*, 2014 *JINST* **9** C05013.

[15] *The Petawatt High-Energy Laser for Heavy Ion EXperiments (PHELIX)*, website visited on 2021-12-11, http://www.gsi.de/en/work/research/appamml/plasma_physicsphelix/phelix.

[16] V. Bagnoud, B. Aurand, A. Blazevic, S. Borneis, C. Bruske, B. Ecker et al., *Commissioning and early experiments of the PHELIX facility*, *Appl. Phys. B* **100** (2009) 137.

[17] B. Akstaller et al., *Single-shot grating-based phase-contrast imaging of a micrometer sample at a laser-driven x-ray backlighter source*, 2021 *JINST* **16** P06021.

[18] S. Schreiner, B. Akstaller, L. Dietrich, P. Meyer, P. Neumayer, M. Schuster et al., *Noise reduction for single-shot grating-based phase-contrast imaging at an X-ray backlighter*, *J. Imaging* **7** (2021) 178.

[19] M. Seifert, M. Weule, S. Cipiccia, S. Flenner, J. Hagemann, V. Ludwig et al., *Evaluation of the weighted mean X-ray energy for an imaging system via propagation-based phase-contrast imaging*, *J. Imaging* **6** (2020) 63.

[20] D.J. Lunn, A. Thomas, N. Best and D. Spiegelhalter *WinBUGS — a Bayesian modelling framework Concepts, structure, and extensibility*, *Stat. Comput.* **10** (2010) 325.

2022 JINST 17 P05033

[21] I. Kawrakow, E. Mainegra-Hing, D.W.O. Rogers, F. Tessier and B.R.B. Walters, *The EGSnrc Code System Monte Carlo Simulation of Electron and Photon Transport*, Tech. Rep., NRCC, Canada (2015), PIRS-701, website visited on 2021-12-25, http://nrc-cnrc.github.io/EGSnrc/doc/pirs701-egsnrc.pdf.

[22] International Commission on Radiation Units and Measurements (ICRU), *Quantities and Units in Radiation Protection Dosimetry. ICRU Report 51* **os26** (1993).

[23] International Commission on Radiation Units and Measurements (ICRU), *Conversion Coefficients for use in Radiological Protection Against External Radiation. ICRU Report 57* **os29** (1998).

[24] J.H. Hubbell and S.M. Seltzer, *Tables of X-ray mass attenuation coefficients and mass energy-absorption coefficients* 1 *keV to* 20 *MeV for elements* $Z = 1$ *to* 92 *and 48 additional substances of dosimetric interest*, Tech. Rep., NIST (1995), NISTIR 5632, http://physics.nist.gov/PhysRefData/XrayMassCoef/cover.html.

[25] S. Schmidt, *Dosimetry and X-ray spectroscopy with the photon counting pixel detector Dosepix*, https://nbn-resolving.org/urn:nbn:de:bvb:29-opus4-174579, 2021.

[26] International Organization for Standardization (ISO), *Radiological protection — X and gamma reference radiation for calibrating dosemeters and doserate meters and for determining their response as a function of photon energy — Part 3: Calibration of area and personal dosemeters and the measurement of their response as a function of energy and angle of incidence*, ISO 4037-3, https://www.iso.org/standard/66874.html, 2019.

[27] P. Ambrosi, G. Buchholz and K. Helmstadter, *The PTB beta secondary standard BSS 2 for radiation protection*, 2007 *JINST* **2** P11002.

[28] R. Behrens and G. Buchholz, *Extensions to the PTB Beta Secondary Standard BSS 2*, 2011 *JINST* **6** P11007 [*Erratum ibid.* **7** (2012) E04001] [*Addendum ibid.* **7** (2012) A05001] [consolidated version: http://www.ptb.de/cms/fileadmin/internet/fachabteilungen/abteilung_6/6.3/f_u_e/bss2cons.pdf].

2022 JINST 17 P05033